

A Fully Actuated Robotic Assistant for MRI-Guided Precision Conformal Ablation of Brain Tumors

Gang Li, Niravkumar A. Patel, Everette C. Burdette, *Life Member, IEEE*, Julie G. Pilitsis, Hao Su, Gregory S. Fischer*, *Member, IEEE*

Abstract—This paper reports the development of a fully actuated robotic assistant for magnetic resonance imaging (MRI)-guided precision conformal ablation of brain tumors using an interstitial high intensity needle-based therapeutic ultrasound (NBTU) ablator probe. The robot is designed with an eight degree-of-freedom (DOF) remote center of motion (RCM) manipulator driven by piezoelectric actuators, five for aligning the ultrasound thermal ablator to the target lesions and three for inserting and orienting the ablator and its cannula to generate a desired ablation profile. The 8-DOF fully actuated robot can be operated in the scanner bore during imaging; thus, alleviating the need of moving the patient in or out of the scanner during the procedure, and therefore potentially reducing the procedure time and streamlining the workflow. The free space positioning accuracy of the system is evaluated with the OptiTrack motion capture system, demonstrating the root mean square (RMS) error of the tip position to be 1.11 ± 0.43 mm. The system targeting accuracy in MRI is assessed with phantom studies, indicating the RMS errors of the tip position to be 1.45 ± 0.66 mm and orientation to be $1.53 \pm 0.69^\circ$. The feasibility of the system to perform thermal ablation is validated through a preliminary ex-vivo tissue study with position error less than 4.3 mm and orientation error less than 4.3° .

Index Terms—MRI-guided robot, ultrasound thermal ablation, robot-assisted neurosurgery, image-guided therapy.

I. INTRODUCTION

BRAIN metastases (BM) are the most common site of metastases from systemic cancer in North America, with approximately 1.7 million American diagnosed with cancer annually [1] and 25% – 40% of them developing BM [2]. Craniotomy can be effective for tissue diagnosis, rapid relief of symptoms, and local disease control, but it is highly invasive and has a 5% risk of complications that can affect quality of life. Stereotactic radio surgery (SRS) or whole brain radiation therapy (WBRT), by contrast, is a non-invasive approach that can improve survival, but symptom relief requires longer than surgery and it does not allow diagnostic confirmation. In addition, non-pathologic tissue at the periphery of a tumor is often radiated, and thereby use of radiation near vital structures (e.g. optic nerve or brainstem) is limited. Thermal ablations, including radio frequency ablation, laser ablation and microwave ablation, offer alternative options that are less invasive than craniotomy but allow for immediate tissue diagnosis, and rapidly lower tumor burden beginning within

2-3 days of treatment and substantially more over a 3-4 week period.

Albeit the significant benefits, delivery of a thermal ablator to a BM lesion accurately and efficiently confers tremendous technical challenges. Existing commercial manual stereotactic frames, such as Leksell (Elekta AB, Sweden) and Radionics CRW (Integra Lifesciences, USA), have to be firmly mounted on the skull requiring multiple incisions. Moreover, manual adjustment of the frame is time-consuming and may introduce instrument placement errors. Robotic stereotactic systems, including NeuroMate (Integrated Surgical Systems, CA) [3], PathFinder (Armstrong Healthcare Ltd, UK) [4], Renaissance (Mazor Robotics, Israel), and Rosa (Medtech Surgical, Inc. France) [5], that integrate planning systems using preoperative medical images could provide precise targeting. But, effective intraoperative imaging is unavailable in these systems. Hence, they cannot compensate for brain deformation that occurs when the skull is opened, which may be shifted by up to 20 mm [6]. Therefore, intraoperative imaging is essential for guiding conformal ablation, providing enhanced safety and accuracy.

MRI is an excellent imaging modality for guiding and monitoring interventional procedures; thanks to its capability to offer real-time high-resolution soft tissue imaging without ionizing radiation. Uniquely, MRI is also able to monitor the temperature and thermal dose through MR thermal imaging (MRTI), which enables real-time feedback for updating a thermal therapy treatment plan as the ablation progresses. Direct MRI guidance during stereotactic cannula delivery would allow for real-time feedback by visualizing the insertion and confirming the placement. ClearPoint (MRI Interventions, Inc., USA) [7], an MRI-guided navigation platform, has been used clinically to provide real-time intraoperative MRI guidance for neurosurgical procedures. Albeit the precise targeting accuracy, it requires the frame to be adjusted manually via a cable driven mechanism, which is time-consuming and ergonomically inefficient. Further, it is mounted to the skull and may require repeated attachment procedures should multiple disparate insertion trajectory be required. NeuroBlate (Monteris Medical, MN), a robotic probe driver, is able to place an MR-conditional laser probe, perform laser interstitial thermal therapy (LITT), and monitor thermal dose using real-time MRI thermometry data. However, it has to be attached to a bolt on the skull and can only provide a 2-DOF motion, i.e. rotation and insertion of the laser probe, which limits its ability to reach various targets through one single entry point and to generate complex ablation profiles. Operating inside of long bore, high-field magnets would clearly benefit from remote actuation. Robotic assistance is therefore introduced into MRI-guided procedures. However, the spatial constraints

Gang Li, Niravkumar A. Patel, and Gregory S. Fischer are with the Automation and Interventional Medicine (AIM) Laboratory in the Department of Mechanical Engineering, Worcester Polytechnic Institute, Worcester, MA, USA (gfischer@wpi.edu)

Everette Burdette is with Acoustic MedSystems Inc., Savoy, IL, USA

Julie G. Pilitsis is with Albany Medical College, Albany, NY, USA.

Hao Su is with the Department of Mechanical Engineering, City College, City University of New York, NY, USA.

* indicates corresponding author.

of operating inside the bore and strict requirements for compatibility with MRI make it difficult to develop robots for such an environment and hence most presently available MRI-guided robots suffer from complex design, bulky size, and kinematic limitations.

The fundamental principal of pneumatic actuation can be MR-safe and cause minimal image degradation, and has been used broadly in MRI-guided robotic systems [8]–[13]. However, its intrinsic nonlinear feature makes it difficult to control, especially when long transmission lines are used. In addition, pneumatic actuators usually have bulky profile, require long air housing, and the shape is distinct from traditional electric motors, which restricts the flexibility of the robot design. Likewise, hydraulic actuation potentially could be MR-safe [14], but it has the potential risk of fluid leakage and cavitation, as well as the inconvenience of having to reset a closed hydraulic system for each use if not permanently installed. Shape memory alloy (SMA) spring actuators have been used to drive an MRI-guided neurosurgical robot, showing no significant visual image distortion [15]. But, theoretical modeling of the behavior of SMA spring actuators is complicated and not accurate. In addition, the actuation speed is slow due to the slow cooling nature of SMA materials in an antagonistic configuration. Nonmagnetic piezoelectric actuation, in contrast, allows high precision targeting with excellent dynamic performance, relative simple control, and a compact profile. NeuroArm (IMRIS, Inc. USA) [16], a teleoperated robotic system consisting of dual dexterous arms driven by piezoelectric motors, was developed to perform both microsurgery and stereotactic procedures with intraoperative MRI guidance. For the sake of performing general purpose procedures, the system was designed with relatively bulky size and thus it needs to be placed outside the scanner bore, which limits its capability of acquiring simultaneous images and robot operation. Literature reviews of robotic systems for neurosurgery include [17], [18].

This study presents an 8-DOF fully actuated robotic assistant that allows in-bore needle-based therapeutic ultrasound (NBTU) placement under intraoperative real-time MRI-guidance, to solve two essential clinical demands, namely accuracy and efficiency. In our previous research endeavors, we have developed a prototype 5-DOF MR-conditional robotic system that acts as an actuated stereotactic frame for alignment of deep brain stimulation (DBS) electrode with manual insertion [19], and the system has demonstrated less than 15% SNR variation and less than 0.20% geometric distortion artifact. In this study, we targeted a new more demanding clinical application, redesigned the original 5-DOF mechanism for the actuated stereotactic frame, and enhanced the design by supplementing it with a newly designed 3-DOF actuated NBTU driver module, enabling a fully actuated mechanism with a compact profile. The fully actuated robot that operates within the MRI scanner bore makes the system capable of utilizing real-time guidance during the procedures; thus, alleviating the need for moving the patient out of the scanner and in turn streamlining the workflow. The 3-DOF motorized NBTU ablator driver module is designed to adjust the position and orientation of the ablator and its cannula individually, allowing

enhanced dexterity and greater control of the ablation profile. First of its kind interstitial high intensity NBTU ablator with embedded active MRI tracking coils is designed to provide conformal directional ablation and intra-operative ablator trajectory confirmation. The primary contributions of this study include: 1) novel design and system integration of an 8-DOF fully actuated conformal/directional NBTU manipulator with piezoelectric actuation, enabling brain tumor ablation inside the closed-bore scanner, as well as simultaneous robot motion and real-time MR imaging, 2) design of interstitial high intensity NBTU ablator with sectored transducers, allowing conformal directional ablation with greater control of ablation profile, 3) design and integration of novel active tracking coils with the US ablator, providing intra-operative trajectory confirmation, and 4) experimental evaluation of active tracking coils localization accuracy and assessment of the system targeting accuracy via free space assessment, MRI phantom studies, as well as preliminary validation of the clinical workflow to perform thermal ablation through ex-vivo tissue thermal treatment studies.

II. INTERSTITIAL HIGH INTENSITY THERAPUTIC ULTRASOUND ABLATOR

In this work we pursue ultrasonic interstitial thermal therapy (USITT), which is distinctly different than LITT and external high-intensity focused ultrasound (HIFU) [20]. Localized heating of tissue with ultrasound interstitial high-intensity thermal therapy is caused by mechanical losses from the propagation of the acoustic waves through the tissue. The longitudinal pressure waves travel through the tissue and have a mechanical force on the molecules, producing oscillatory motion at the applied 5-10MHz. The frictional losses produce heating of the tissue. The energy propagates through the tissue with a $1/r$ relationship, where r is the distance from the ablator; it achieves significant penetration, but the short wavelength also permits steering and excellent directivity. The nature of coagulation produced is consistent throughout the lesion, without charring or vaporization, as is commonly produced using other thermal techniques. Consistent heating/ablation allows the ablator to be easily removed from the tissue without causing tissue damage from retraction. Propagation is dependent on acoustic properties of the tissue, which vary less across tissues than electrical conductivity. For comparison, RF ablation (RFA) power density at the electrode is greatest and decays with a $1/r^2$ relationship, and it cannot be directionally controlled. RFA heating is highly dependent upon predominantly thermal conduction; thus charring of tissue around the electrode probe is often the result. LITT has very limited penetration in tissue and is also predominately dependent upon thermal diffusion.

The ACOUSTx NBTU ablator (Acoustic MedSystems Inc., Savoy, IL) developed by our collaborator [21], [22] is an interstitial high intensity therapeutic ultrasound based ablator. In this study, we designed an MR-conditional variant of the ablation instrument with MR-conditional materials and an improved configuration intended to operate within the scanner bore, as shown in Fig. 1. The ACOUSTx ablator contains 1 to 4 tubular ultrasound transducers (each of 5 to 11mm

length, and 1.5mm diameter), which are made of piezoelectric ceramics and mounted on a hollow polyimide tube, ensuring the compatibility with MRI environment. The ablator is attached to a plastic implant catheter to enable circulation of degassed water cooling flow to couple the ultrasound, improve thermal penetration, and cool the transducers. The transducers are fabricated with sectored shape and individually powered with an adjustable intensity and heating time interval, to provide a specific angular acoustic region or directional conformal ablation at the periphery of a target region, selectively destroying the target tissue while preserving critical tissue. The biothermal and acoustic models of the ultrasound ablator was reported in [22], which described how the ablation zone can be controlled. Use of sectored transducers would enable conformal directional ablation with greater control of the ablation zone shape, size, and volume. This would improve the treatment margin and limit the risk of damaging nearby normal tissue. For delivery of the flexible ablator, a rigid cannula is inserted first into the brain tissue to provide a straight pathway for the ablator and reduce the bending, as depicted in Section IV-C.

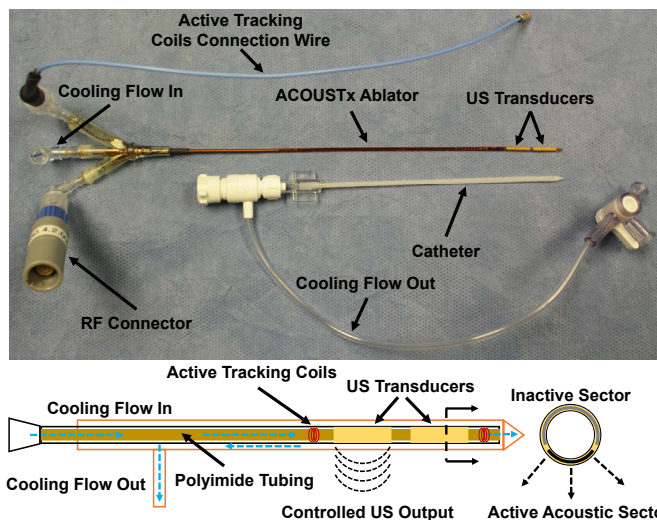


Fig. 1: (Top) ACOUSTx needle-based therapeutic ultrasound (NBTU) ablator in a configuration with two separate transducer sections along the axis of the instrument. The ablator is designed to be inserted within a plastic implant catheter to prevent from bending, as well as return the water flow. (Bottom) Schematic diagram of the US ablator in a configuration with two 90° directional acoustic sectors, labeled as the US transducers, and two solenoid coils on both ends.

III. ACTIVE TRACKING COILS

Precise localization of the ablator is essential for confirming the desired ablator trajectory. To localize the ablator during MR imaging, novel active tracking coils are designed and embedded along the ablator shaft, which consisted of two small solenoid coils and one on each end of the transducers, as illustrated in Fig. 1. Using those two coils, not only ablator tip location but also ablator orientation can be obtained. Water circulated through the ablator for transducers cooling enables MRI-based localization even when the ablator is in free air.

The physical dimensions of the tracking coils are constrained by the compactness of the ablator itself. The catheter has an outer diameter of 2.4mm, which houses the ablator with outer diameter of 1.4mm. The ablator has an inner tube with diameter of 0.5mm for water circulation, the tracking coils are wound on this inner tube using 40AWG copper wire. Both coils have 5 turn windings and are approximately 0.6mm long, placed in series connection. Signal from the coils are carried by the twisted pair leads, transitioning to a 1.4mm diameter 50Ω coax at the connector elbow. Both coils interface to the scanner through a compact custom tuning box that resides near the ablator and a custom interface box adapted from an existing coil interface for 3T scanner (Achieva, Philips, Netherlands).

To achieve high accuracy localization of tracking coils and consequently of the ablator, a T1-weighted fast field echo (T1-FFE) scan sequence with 2D projections is devised (slice thickness: 320mm, pixel spacing: 0.39mm x 0.39mm, number of echoes: 2, flip angle: 10°, TR: 29.82ms, TE: 8.125ms, scan duration: 30.2s). The water cooling flow is stopped during this particular scan to eliminate any motion artifacts. The scan sequence is created such that in each of the R (right), A (anterior) and S (superior) directions, there are two echoes recorded with opposite reading directions. The most simple algorithm is to find peaks and take average of their positions in both echoes, but to improve the accuracy, an algorithm which utilizes image intensities around the tracking coil to better estimate the center of the coils is developed. Fig. 2 shows one of the images and subsequent image processing steps performed to localize the coils. Information from all 6 slices is combined to give precise position of each of the coils, which is used to calculate ablator position and orientation.

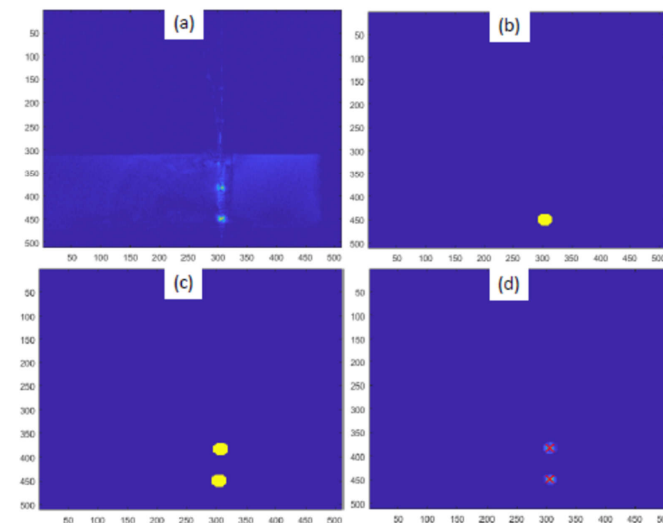


Fig. 2: Image processing steps for tracking coils localization (a) original image, (b) mask for first tracking coil, (c) mask containing both the tracking coils and (d) calculated coil locations overlaid with red cross marks. Unit: pixel (pixel spacing: 0.39mm x 0.39mm)

IV. MECHANICAL SYSTEM DESIGN

A. Design Requirements

The robot manipulator is designed to place the US thermal ablator via a fixed burr hole on the skull while the patient is lying inside the high-field closed-bore MRI scanner in supine position. Since the patient setup is similar to the aforementioned system for DBS [19], a mechanism with equivalent kinematic configuration is adopted in this application and improved with a novel 3-DOF actuated ablator driver module. Hence, as shown in Fig. 3, the manipulator is able to provide 8-DOF motion to deliver and operate the ablator inside the brain: 3-DOF Cartesian motion to position the ablator to target lesion, 2-DOF remote-center-of-motion (RCM) rotary motion to orient the ablator around target lesion, and 3-DOF manipulation of the ablator and cannula to place and orient the directional transducers towards the treatment foci. In clinical use, the first 5-DOF are actuated to align the probe like a traditional stereotactic frame and then locked for the remainder of the procedure, while the 3-DOF end effector are then used to place the cannula and the probe. The 8-DOF motion enables fully actuated placement of the ultrasonic ablator, eliminating the need of moving the patient in and out of the scanner during the procedures and thus streamlining the clinical workflow. In addition, the 3-DOF actuated ablator module is able to adjust the position and orientation of the directional transducers independently along with actuated setting of the delivery cannula depth, and therefore enables control of the ablation profile to match the tumor geometry while minimizing the damage to the surrounding normal tissue. The joint space kinematic specifications are summarized in Table I.

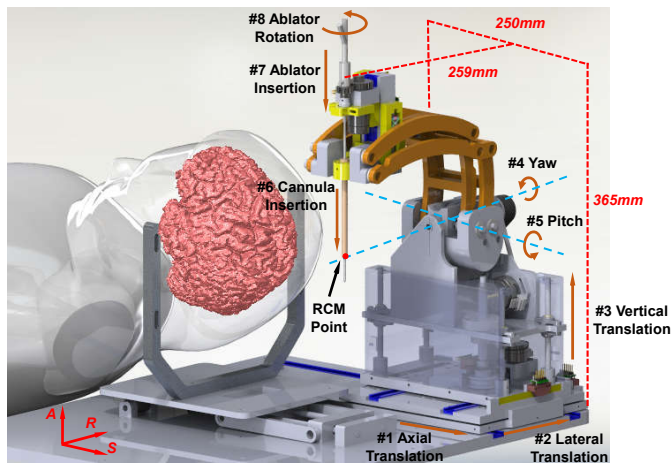


Fig. 3: 3D CAD model of the ultrasonic ablator manipulator, showing the kinematic configuration of degrees of freedom modeled after those of a traditional stereotactic frame and its dimensions at home position.

In terms of materials, three main factors are considered: compatibility with MRI, stiffness, and sterilizability. MRI scanners generate high magnetic and pulsed radio frequency field during imaging, which cause significant challenges to the design of mechanisms with regard to aspects of MRI compatibility. To be compatible with an MRI environment, ferromagnetic materials have to be averted completely, and

non-ferrous electrically conductive materials could be used with caution to limit eddy current generation and resonance. The linkages are machined with an MR-safe and high-stiffness Ultem material (Polyetherimide, flexural modulus 1,300,000 pounds per square inch (PSI)). The major body of the robot is made of 3D-printed ABS plastic (flexural modulus 304,000 PSI). With regard to sterilizability, components that are in direct contact with the patient and part of the sterile kit are made of a sterilizable and bio-compatible material MED610 (Stratasys, MN). The rest of the robot is designed to be draped with sterile plastic cover to create a sterile environment.

With regard to aspects of actuation method, nonmagnetic piezoelectric actuators have proved to be able to provide high precision positioning and with no introduced visible imaging noise with our custom-developed MR-conditional robot controller [19], [23], [24]. In this study, a rotary piezomotor is used to drive the ablator rotation (Piezo LEGS LR5012C, PiezoMotor AB, Sweden). Linear piezomotors (Piezo LEGS LL1011C, PiezoMotor AB, Sweden) and rotary Shinsei motors (USR60-S4N, Shinsei Corp., Tokyo, Japan) are utilized to provide linear and rotary actuation, respectively, for the remaining degrees of freedom.

B. Ablator Positioning and Alignment Module

The mechanism of the 5-DOF ablator positioning and alignment module is redesigned based on the previous study [19] to increase the stiffness and actuation power, and is designed to support the additional 3-DOF ablator driver module that is added on top of the manipulator. The translations of the base stage in the horizontal plane (DOF #1 and #2, as labeled in Table I) are driven directly by the linear Piezomotor via linear sliders. The vertical translation is provided by four aluminum linear guides, which are supported by two solid brackets and lifted via the lead screw-nut mechanism that is actuated by the rotary Shinsei motor through a timing belt (DOF #3). Compared to study [19], Shinsei motor is used in this study for the rotation axes, since it can provide more torque.

RCM mechanisms are commonly used by surgical robots to orient surgical tools inside the patient's body through a fixed entry point. In this study, the RCM mechanism is adopted and configured in the structure of a parallelogram linkage to implement the yaw (DOF #4) and pitch (DOF #5) motions, which are driven by rotary Shinsei motors via timing belt. The rotation axes of yaw and pitch intersect with the ablator insertion axis at a mechanically constrained single point, i.e. the RCM point, making it kinematically equivalent to the arc angles of a conventional stereotactic frame. The linkages of the RCM mechanism are made of high-stiffness Ultem material and fabricated with high-precision CNC machine to achieve high-stiffness structure. Compare to the previous study, the stiffness of the mechanism is also increased through improving the design of several individual components, such as combining separated components into a single solid part, adding support material, and increasing thickness.

C. Ablator Driver Module

A rigid cannula is utilized to guide the ablator into the brain, preventing the ablator from bending during insertion.

The cannula is attached to the cannula guide and inserted robotically by a linear Piezomotor via a linear guide (DOF #6). The ablator is fixed to the driver through the ablator clamp, and inserted robotically (DOF #7) by a linear Piezomotor directly, and rotated (DOF #8) by a rotary Piezomotor through the gears, as shown in Fig. 4 (a). The insertion (DOF #7) and rotation (DOF #8) of the ablator enable control of the position and orientation of the directional transducers to generate a desired ablation profile.

During the clinical procedures, the ablator driver module and the rest of the robot will be covered by a sterile drape. The gears, ablator clamp, and cannula guide, which are in direct contact with the patient, are made of bio-compatible material MED610 and are intended to be sterilized by EtO method, as illustrated in Fig. 4 (b) and (c). A sterile kit, comprising the ablator, gear, ablator clamp with screws, cannula guide with screws, and an MR-conditional screw driver, is utilized to assemble the sterilized components to the ablator driver once the sterile field has been created.

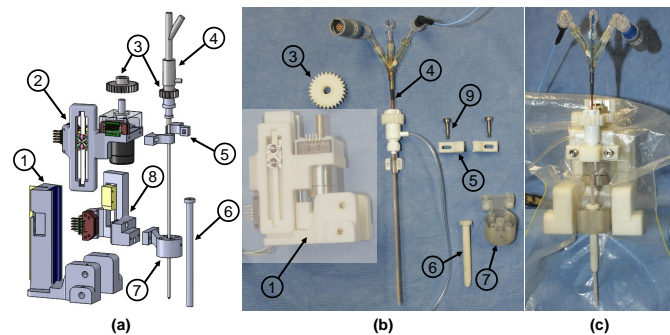


Fig. 4: 3-DOF ablator driver module. (a) exploded view showing: 1) driver base 2) ablator insertion stage 3) gears 4) ablator 5) ablator clamp 6) cannula 7) cannula guide 8) cannula insertion stage 9) thumb screws, (b) components in the semitransparent block are covered with a sterile drape and the remaining parts are made of bio-compatible and sterilizable materials, and (c) assembly of the ablator driver covered with a sterile plastic drape.

D. Head Frame Adjustment Module

The head fixation is performed by a head frame adjustment module which is attached to the base platform of the robot. The head frame adjustment module is designed with a tilt DOF in the sagittal plane, to facilitate insertion of the ablator from varying entry points between forehead and occiput, as shown in Fig. 5. A commercially available MR-conditional Stereotaxy frame (UCHRA, Integra LifeSciences Corporation, NJ) is utilized to secure the head via point-set-screws, preventing the head movement during the procedure. Angulation of the head frame is implemented by a scissor mechanism driven by a manually adjusted lead screw-nut mechanism, which transmits linear motion to angulation.

A removable fiducial frame is repeatedly attached to the platform through locating pins and thumb screws during the registration phase. The fiducial frame consisted of nine tubes filled with MRI-visible high-contrast fluid (Beekley, Bristol, CT), and arranged in a Z pattern in each of the three orthogonal

planes. Based on imaging the fiducial frame, the 6-DOF position and orientation of the robot can be localized with respect to the patient coordinates. The robot base is physically fixed in the platform with known offset from the fiducial frame. Hence, the registration is only performed once during the procedure. Once the robot is registered, the fiducial frame would be removed from the platform to free up the workspace and reduce potential collision with the ablator manipulator. Fig. 14 shows the system setup inside the scanner as the fiducial frame is removed and the ablator manipulator is locked onto the platform.

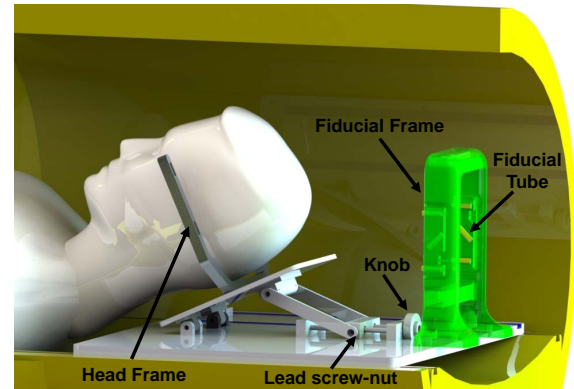


Fig. 5: CAD model of the head frame adjustment module with patient placed in supine position and the fiducial frame attached to the platform. The robot sits beside the patient's head attached to the platform. Note that the fiducial frame is designed to be attached proximal to the head during the registration phase of the procedure; in this figure it is intentionally located at the end of the platform to clearly demonstrate the head frame.

V. KINEMATICS AND REGISTRATION

The robot kinematics are analyzed based on Denavit-Hartenberg (D-H) parameters. The D-H frame assignment is illustrated in Fig. 6, and the D-H parameters are summarized in Table I. Note that, the lowercase letters represent variables that can be actuated by the manipulator, and uppercase letters represent constant values that are determined by the mechanism. The origin of the robot frame, F_{Rob} , is defined at the robot platform with x-y-z axes aligned with the scanner's RAS coordinate system. The base frame, F_{Base} , is defined as the RCM point when the robot is at its home position, with x-y-z axes aligned with the robot frame, F_{Rob} . The tip frame, F_{Tip} , is defined at the tip of ablator, with z-axis pointing along the ablator's longitudinal axis, x-axis aligning with the robot frame, and y-axis determined by the right hand rule. The forward kinematics of the manipulator can be calculated based on the homogeneous transformation chain, depicted as:

$$\begin{aligned}
 T_{Tip}^{Base} &= T_{Rob}^{Base} T_{Tip}^{Rob} \\
 &= T_{Rob}^{Base} T_1^0 T_2^1 T_3^2 T_4^3 T_5^4 T_6^5 T_7^6 T_8^7 \\
 &= \begin{bmatrix} nx & sx & ax & px \\ ny & sy & ay & py \\ nz & sz & az & pz \\ 0 & 0 & 0 & 1 \end{bmatrix} \quad (1)
 \end{aligned}$$

$$P = \begin{bmatrix} px \\ py \\ pz \end{bmatrix} = \begin{bmatrix} d_2 + d_6 \cos \theta_5 + d_7 \cos \theta_5 \\ d_3 + d_6 \sin \theta_4 \sin \theta_5 + d_7 \sin \theta_4 \sin \theta_5 \\ d_1 + d_6 \cos \theta_4 \sin \theta_5 + d_7 \cos \theta_4 \sin \theta_5 \end{bmatrix} \quad (2)$$

$$A = \begin{bmatrix} ax \\ ay \\ az \end{bmatrix} = \begin{bmatrix} \cos \theta_5 \\ \sin \theta_4 \sin \theta_5 \\ \cos \theta_4 \sin \theta_5 \end{bmatrix} \quad (3)$$

Where T_{Tip}^{Base} is the ablator tip frame with respect to the base frame, T_{Tip}^{Rob} is the tip frame represented within the robot frame, T_{Rob}^{Base} is constant offset from the robot frame to the base frame, P is the ablator tip position (origin of the tip frame F_{Tip}), and A is the vector along the ablator longitudinal axis (z-axis of F_{Tip}).

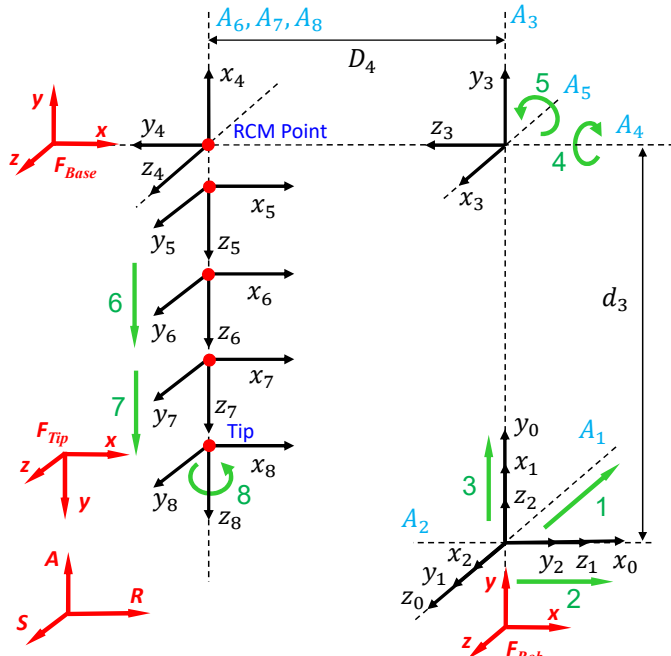


Fig. 6: D-H frame assignment of the 8-DOF ablator manipulator. The origin of robot frame F_{Rob} is defined at the robot platform with x-y-z axes aligned with scanner’s RAS frame. The base frame F_{Base} is defined as the RCM point at home position. The tip frame F_{Tip} is defined at the tip of the ablator, with z-axis pointing along the ablator’s longitudinal axis.

TABLE I: D-H Parameters of Robot Manipulator

Axis	Motion	l_i	α_i	d_i	θ_i	Range
1	Axial	0	90	d1	90	0~50mm
2	Lateral	0	90	d2	90	0~40mm
3	Vertical	0	90	d3	0	0~50mm
4	Yaw	0	90	D4	θ_4	0~90°
5	Pitch	0	90	0	θ_5	-45~45°
6	Cannula Insertion	0	0	d6	0	0~40mm
7	Ablator Insertion	0	0	d7	0	0~30mm
8	Ablator Rotation	0	0	0	θ_8	-180~180°

Kinematically the RCM point can lie along the axis of the ablator resulting in an infinite number of inverse kinematics

solutions. In this study, to simplify the kinematics, the ablator tip is defined at the RCM point. The ablator tip location is determined by finding the center of the lesion and then applying the known tip offset from the center of the active US transducer along the ablator axis and the cannula is inserted 30mm proximal to the ablator tip. Therefore, d_6 and d_7 are constant values for a given ablator design, i.e. $d_6 = D_6, d_7 = D_7$ (D_6, D_7 are constants determined by the length of the ablator and cannula). However, for different applications the relation between cannula and ablator can be variable, and additional flexibility in path planning may be afforded by using a variable d_6, d_7 , which beyonds the scope of this study. Ablators and cannulas with varying lengths may be adopted for different target foci. The rotation of the ablator θ_8 is an independent control input determined by the tumor geometry, which could be defined by optimizing the thermal treatment shape and not discussed in the kinematics of this study. To solve the inverse kinematics, the ablator tip position P and vector A are identified with respect to the MR image volume as part of the surgical planning process. By defining $d_6 = D_6, d_7 = D_7$, the inverse kinematics can be written as:

$$\begin{aligned} d_1 &= pz - D_6 \cos \theta_4 \sin \theta_5 - D_7 \cos \theta_4 \sin \theta_5 \\ d_2 &= px - D_6 \cos \theta_5 - D_7 \cos \theta_5 \\ d_3 &= py - D_6 \sin \theta_4 \sin \theta_5 - D_7 \sin \theta_4 \sin \theta_5 \\ \theta_4 &= \text{atan2}(ay, az) \\ \theta_5 &= \text{acos}(ax) \\ d_6 &= D_6 \\ d_7 &= D_7 \end{aligned} \quad (4)$$

As described in Section IV-D, fiducial frame based registration is utilized to register the robot to the scanner RAS coordinate system. Images of the fiducial frame are acquired to calculate the robot registration transform using line marker registration [25]. The calculated registration transform is sent over a network connection via OpenIGTLink [26] to the robot control software, to solve the 6-D ablator tip pose in patient coordinates through the transformation chain, written as:

$$T_{Tip}^{RAS} = T_Z^{RAS} T_{Base}^Z T_{Tip}^{Base} \quad (5)$$

Where T_{Tip}^{RAS} is the ablator tip pose represented within the RAS coordinate system, T_Z^{RAS} is the fiducial frame pose with respect to the RAS coordinate system determined by the registration, T_{Base}^Z is the constant offset from the robot base to the fiducial frame, and T_{Tip}^{Base} is the ablator tip position with respect to the robot base, as determined by the robot kinematics.

The workspace of the manipulator is designed to cover the typical foci of brain tumors, i.e. frontal lobe, parietal lobe, occipital lobe, and temporal lobe. According to the anthropometry [27], [28], the dimensions of 95% male bitracion breadth, head length, and stomion to top of head are 15.5cm, 20.9cm, and 19.9cm, respectively. The range of motion for each axis is summarized in Table I, and the workspace is analyzed based on the robot kinematics. For custom NBTU ablaters with 100mm length variation, the robot could reach a volume of 181.4mm along R-axis, 150mm along A-axis, and 150mm along the S-

axis, which is sufficient to cover typical foci of brain tumors, as illustrated in Fig. 7.

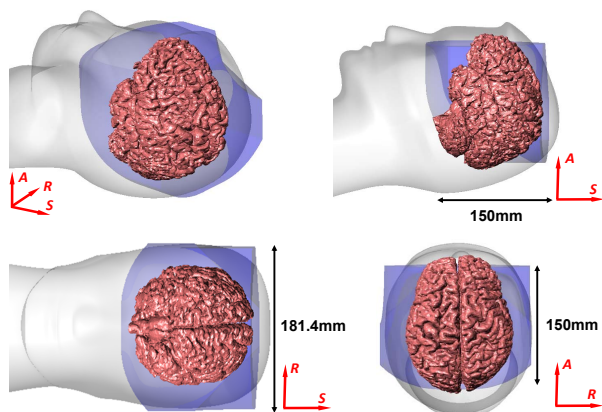


Fig. 7: Reachable workspace of the robot overlaid on a representative human brain.

VI. EXPERIMENT AND RESULTS

Four sets of experiments were performed to evaluate the system positioning accuracy, active tracking coils localization accuracy, and to validate the clinical procedure workflow: 1) System positioning accuracy was first assessed in free space with an OptiTrack motion capture system, and 2) further assessed in task space with MRI phantom studies. 3) Active tracking coils localization accuracy was evaluated in free space with MR images. 4) Finally, a preliminary study of thermal ablation under MRI-guidance was conducted - this included both ex-vivo chicken breast tissue and a lamb brain to evaluate the clinical workflow. Three metrics were employed to analyze the system positioning errors, i.e. tip position error, insertion angle error, and RCM intersection error. Tip position error is determined as the distance from the desired target to the actual ablator tip position. Insertion angle error is a measure of an angular error between the planned needle insertion angle and the actual needle insertion angle. RCM intersection error is measured as the distance between the RCM intersection point and needle insertion axes, indicating the mechanism's performance as a RCM device.

A. Clinical Procedure Workflow

The proposed image-guided robot-assisted clinical workflow is based on a conventional stereotactic neurosurgery approach using a Leksell-type manual frame in order to minimize clinical complications and streamline the design procedures. As shown in Fig. 8, the workflow is composed of following major steps:

- 1) Make incision and burr hole based on modifications of Kocher's point according to the target site.
- 2) Initialize the hardware and software of the robotic system.
- 3) Fiducial frame registration: register the robot to the MRI scanner coordinate system with a fiducial frame.
- 4) Patient positioning: place the patient in the scanner with supine position and fix the head.
- 5) Localize skull entry points.

- 6) Surgical site preparation: create sterile environment for the scanner, surgical site on the patient, and the robot manipulator.
- 7) Cannula alignment: align the delivery cannula and insert through the entry point.
- 8) US ablator placement: insert the ablator through the cannula to the desired target.
- 9) Trajectory confirmation: confirm the ablator trajectory with active tracking coils that align with the ablator axis.
- 10) Ablation treatment: perform thermal ablation via treatment planning software, TheraVision, under real-time MR thermal imaging monitoring.
- 11) Finalization: retract the ablator and cannula, close the incision, and remove the patient.

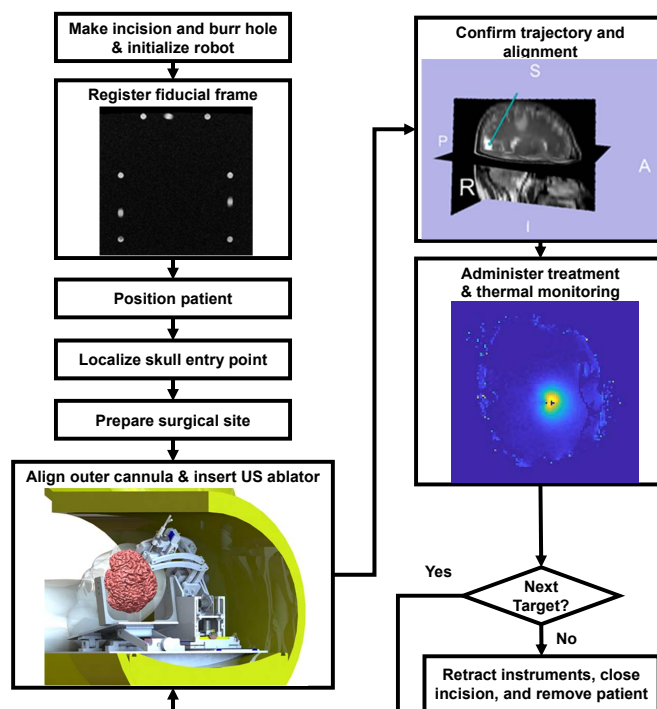


Fig. 8: Clinical workflow of MRI-guided robot-assisted thermal ablation of brain tumors.

B. Free Space Positioning Accuracy Evaluation

The free space positioning accuracy was conducted with a 6-camera OptiTrack motion capture system (Flex 13, NaturalPoint, OR, USA). The resolution of the camera is 1.3MP (1280x1024) and it can typically track with our configuration at 0.2mm. A 6-D reference marker frame was firmly mounted on the robot platform, and a 6-D tracking frame was attached to the needle driver, as shown in Fig. 9. The robot was translated to six target locations, and orientated to five different angulations at each target location, resulting in 30 poses in total that covers the major workspace of the robot. The 6-D actual pose was measured by the OptiTrack system, and registered to the desired targets with point cloud based registration to eliminate registration-related errors in this stage of the validation process. The experimental results demonstrate that the root mean square (RMS) error of the tip position is 1.11 ± 0.43 mm, insertion angle error is $1.19 \pm 0.52^\circ$,

and the RCM intersection error is 0.27 ± 0.06 mm. The RMS errors of the position and orientation in each axis are x-axis (0.35mm), y-axis (0.62mm), z-axis (0.85mm), Yaw-axis (0.46°), and Pitch-axis (1.10°). The results indicate that the errors in different axes are within the same magnitude with small variations. The errors in Pitch-axis are higher than other axes, which is mainly due to the alignment errors of the linkages. Clearances between the shafts and holes on the linkages were observed, due to the manufacturing tolerance, which causes misalignment errors and angular variation as the linkages extend or retract about the Pitch-axis.

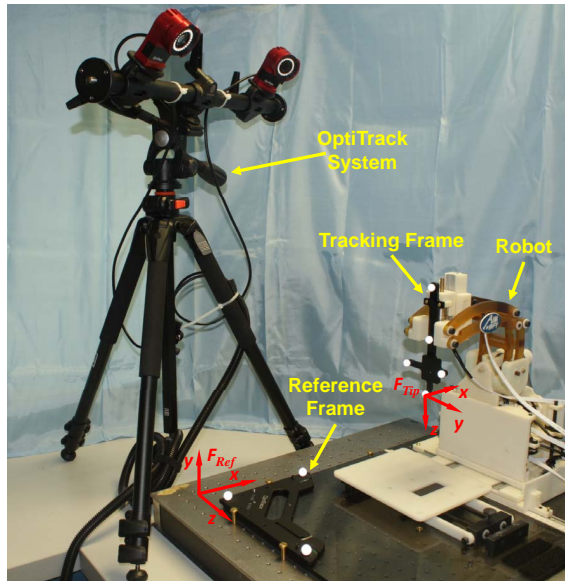


Fig. 9: Experimental setup of free space accuracy evaluation with OptiTrack motion capture system. Note that, six identical cameras are used in this study to capture the 6-D needle pose, and only two of them are visible in this figure.

C. System Accuracy Evaluation with MRI Phantom Studies

The system level accuracy was assessed with phantom studies inside a 3T MRI scanner (Achieva, Philips, Netherlands), with equivalent setup as shown in Fig. 14. To isolate needle deflection related errors from robotic system accuracy, a stiff 13-gauge brass needle with rounded flat tip was inserted into a gelatin phantom (Knox, Kraft Foods, IL) and imaged with a T2-weighted turbo spin echo (T2W-TSE) imaging protocol (TE: 115ms, TR: 3030ms, flip angle: 90° , slice thickness: 3mm, pixel spacing: $0.46\text{mm} \times 0.46\text{mm}$) to measure the actual needle trajectories. Three RCM tip locations were virtual (i.e. pixel coordinates in the image) and randomly selected in the MR images across the workspace and targeted from five different orientations at each location, resulting in 15 needle insertions in total. The actual trajectory of each needle insertion was manually segmented and measured from MR images and compared to the desired targets to analyze the system accuracy. The experiment results demonstrate that the RMS error of the tip position is 1.45 ± 0.66 mm, orientation error is $1.53 \pm 0.69^\circ$, and the RCM intersection error is 0.75 ± 0.33 mm. Fig. 10 illustrates the accuracy results of one representative target location with five different orientations.

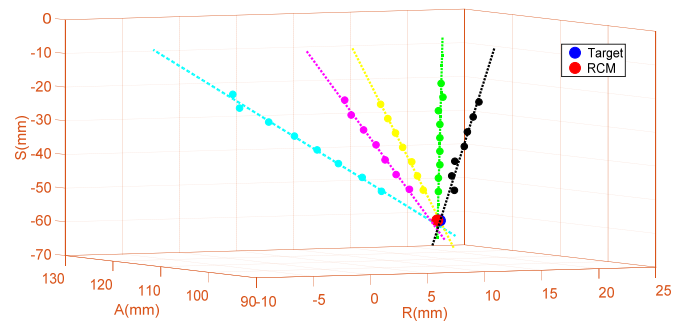


Fig. 10: A representative plot of five insertion pathways intersecting at a given target location based on the segmentation of MR image data. For the total 15 trials, the RMS error of the tip position is 1.45mm, orientation error is 1.53° , and RCM intersection error is 0.75mm.

D. Active Tracking Coils Localization Accuracy Evaluation

Accuracy evaluation of the active tracking coils localization was performed with a 3D printed template, allowing the ablator to be inserted at various angles. The template is designed such that all the insertions intersected at a common point, mimicking the RCM mechanism as described in Sec. IV-B. As shown in Fig. 11, the ablator was inserted into the guiding hole and a coil tuning box was connected to the ablator to acquire signals from the active tracking coils. The fiducial frame described in Sec. IV-D was utilized for initial localization of the template in MR image space. To evaluate the accuracy of the ablator localization algorithm, all insertions were performed in air minimizing any possible deflection due to probe bending. Tracking coil sequence aforementioned in Sec. III was utilized to acquire two echoes in three projection images, giving locations of the tracking coils in RAS coordinates. Image processing algorithm described in Sec. III was used to localize the tracking coils and calculate ablator position and orientation. Fig. 12 shows plot of tip errors in RAS coordinates with RMS error less than 1.1mm and orientation errors around R-axis and S-axis with RMS error less than 2.3° . The plot indicates that the localization accuracy of tracking coils is affected by the angle between the B_0 magnetic field and probe axis orientation. With the angle about the R-axis around 60° (the primary intended operating region), it has minimal errors. In addition, error is attributable to manufacturing tolerance (template manufacturing tolerance, guide hole clearance, tracking coils assembly errors, etc.), undesired ablator probe bending, and imaging resolution.

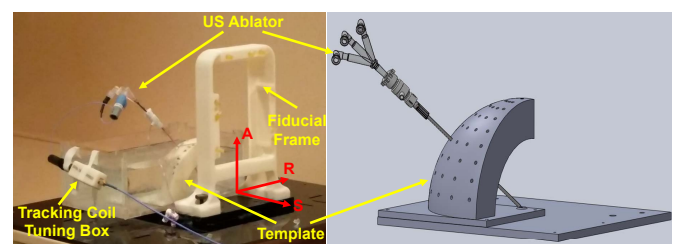


Fig. 11: Experiment setup of active tracking coils localization showing 3D printed template, ablator inserted through one of the guiding holes, and the tracking coil tuning box.



Fig. 12: Ablator localization results showing position errors in R, A and S axes and orientation errors around R-axis and S-axis. The RMS errors of tip position less than 1.1mm and orientation less than 2.3° .

E. Preliminary Study of Thermal Ablation Within Ex-vivo Tissue

The feasibility of the system to perform thermal ablation treatment was validated through a preliminary ex-vivo tissue study. A fresh chicken breast tissue was firstly employed as a specimen, since the ablation treated foci could create visible changes from the normal tissue, which can be used to identify and inspect the ablation treatment. The chicken breast was molded into a gelatin phantom to reduce tissue movement during the insertions. An US ablator with a 90° active sector was utilized to perform the ablation treatment. Two target locations were virtual (i.e. pixel coordinates in the image) and randomly selected inside the ex-vivo tissue and treated with US thermal ablation. The position and orientation errors for the two insertions are 3.5mm, 3.9° and 4.3mm, 4.3° respectively. The errors are calculated as the differences between the desired targets and actual needle tip positions, which are acquired from the MR images and measured in patient coordinates. Fig. 13 shows the treated tissue with thermal ablation. The ablation profile is uniform within the active angular sector and length of the transducer. Longitudinal energy pattern conforms well to length of active transducer and width of the angular sector.

For workflow evaluation in a scenario mimicking soft brain tissue of a patient, a lamb head was fixed on the head frame and set to an appropriate orientation via the head frame adjustment module. An US ablator with a 180° active sector was utilized to perform the ablation treatment. One target in the lamb brain was placed by the robot. The experiment setup is shown in Fig. 14, and the ablator track in the lamb brain is visualized on MR images as illustrated in Fig. 15. There was no visible imaging quality degradation observed during the experiment. The position and orientation errors for the insertion are 0.5mm and 2.0° respectively. The experiment indicates that the placement errors in the chicken breast muscle are higher than that in the lamb brain. The main cause is that the stiffness of the chicken breast is higher than lamb brain, which leads to deflection of the ablator and thus placement errors that we do not anticipate to be significant in the soft brain tissue of patients.

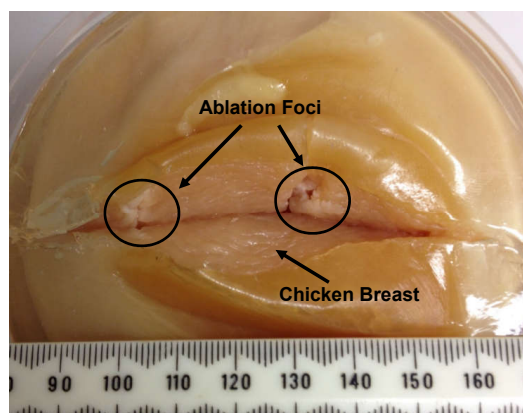


Fig. 13: Ex-vivo chicken breast tissue with two thermal ablation foci about 30mm apart. The chicken breast tissue is modeled into a gelatin phantom to reduce movement during the insertions. The tissue is cut open right after the experiment to inspect the ablation treated foci, which has visible changes from the normal tissue, i.e changing to solid white color in the direction of the active ultrasound sector.

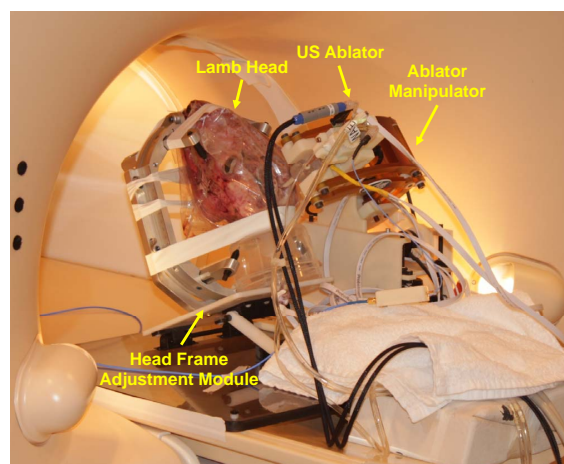


Fig. 14: Experimental setup for ultrasound-based thermal ablation on an ex-vivo lamb brain. The lamb head is fixed at the head frame adjustment module via screws to prevent head movement during the procedures. The NBTU ablator is placed by the robot manipulator locked in place on the side.

VII. DISCUSSION AND CONCLUSION

This study reports the development of an 8-DOF fully actuated robot assistant for ultrasonic thermal ablation of brain tumors under intraoperative MRI-guidance that addresses two unmet essential clinical demands: accuracy and efficiency. The experimental results of system targeting accuracy in MRI phantom studies demonstrate RMS tip position error is 1.45 ± 0.66 mm, orientation error is $1.53 \pm 0.69^\circ$, and RCM intersection error is 0.75 ± 0.33 mm. Error of the preliminary ex-vivo tissue study are less than 4.3mm and 4.3° . The results of the accuracy studies are summarized in Table. II. The targeting accuracy of MRI phantom studies is comparable to the relevant study on robot assisted needle access of brain (1.55mm) [13]. In addition, considering the diameter of the primary tumors are around 4cm [29], the targeting accuracy less than 5mm coupled with the directional conformal ablation ability of our system should be sufficient for the application. Error sources

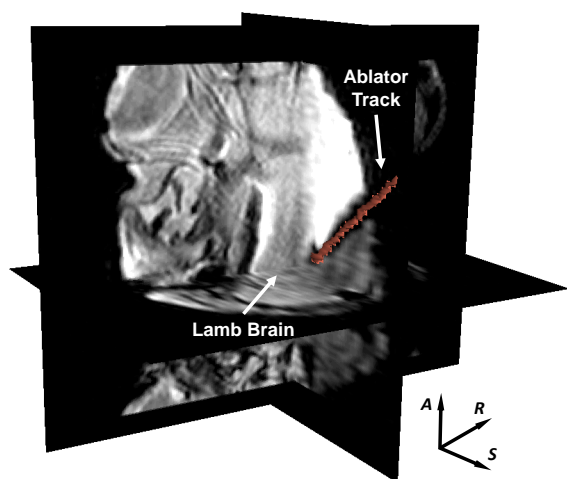


Fig. 15: 3D MR image volume showing the US ablator inserted inside an ex-vivo lamb brain. The red line represents the actual US ablator segmented from MR volume images.

include robot mechanism errors (i.e. manufacturing tolerance, assembly misalignment, deformation of 3D printed plastic material, backlash of the timing belt etc.), imaging-related errors (i.e. imaging resolution, registration errors, etc.), and deflection of the ablator. The error contributions of the robot mechanism and imaging-related factors could be identified through the free space evaluation and MRI phantom studies, respectively. The major reason of having larger error in ex-vivo tissue than free space and phantom is because the ablator is flexible and is deflected while being inserted into the ex-vivo tissue, especially for the chicken breast tissue which has a much higher stiffness than brain tissue. This prototype design is made in part of 3D printed plastic materials for rapidly validating feasibility and initial accuracy analysis. Plastic deformation and manufacturing-related errors lead to inaccurate alignment of joint axes, deformation of the pivot location, and variation of RCM center point. These are being addressed in preparation for the next clinical iteration of the robot, including replacing the 3D printed plastic materials with precision machined Ultem to improve stiffness and accuracy. Active tracking coils localization is studied in free space for ablator trajectory confirmation. In this study, the probe was placed within 0 - 90° quadrant for both the R and A axis rotations. The error characteristics of tracking coils might depend on the quadrant in which the probe is placed. Further study would be performed in the future work to evaluate the localization accuracy which would include other position orientations.

TABLE II: Summary of Accuracy Studies Results

Experiment	Tip Positon Error (mm)			Orientation Error (deg)		
	RMS ± SD	Max	Min	RMS ± SD	Max	Min
Free Space	1.11 ± 0.43	1.96	0.31	1.19 ± 0.52	3.31	0.20
MRI Phantom	1.45 ± 0.66	3.01	0.19	1.53 ± 0.69	2.73	0.50
Chicken Breast	3.9 ± 0.4	4.3	3.5	4.1 ± 0.2	4.3	3.9
Lamb Brain		0.5			2.0	

With regard to the efficiency, fully actuated mechanism design eliminates time-consuming iterative manual adjustment

and alleviates the need for repeatedly moving the patient in and out of the scanner during the procedure. In terms of safety, the sectored transducers are able to provide directional conformal ablation at the periphery of a target region, selectively destroying the target tissue while preserving critical tissue. The 3-DOF ablator driver enables conformal directional ablation with greater control of the ablation zone shape, size, and volume, and would improve the treatment margin and limit the risk of damaging nearby healthy tissue. Further study would be conducted to optimize the monitoring and control of ablation profile and thermal dose, as well as further address safety to enable a safe robot-assisted NBTU placement procedure.

The system is evaluated in free space, MRI with a phantom, and preliminary ex-vivo studies; a comprehensive evaluation with animal and cadaver studies to validate the targeting accuracy, clinical workflow, and procedure time is forthcoming. The imaging quality degradation is validated qualitatively; a thorough quantitative MRI compatibility evaluation, such as the SNR analysis, will be performed prior to clinical studies. For the preliminary study of thermal ablation, we only evaluated the placement accuracy of the ultrasound ablator and did not consider the ablation accuracy. One potential solution in our ongoing research is using MRTI to monitor the actual thermal dosage in real-time and to compare it with the desired ablation zone shape. Moving forward, integration with continuous intraoperative MRI (ioMRI) guidance developed in our previous research efforts [30] would enable intraoperative visualization of brain anatomy and compensation for ablator placement errors and brain shift.

ACKNOWLEDGEMENTS

This work is supported by NIH NCI Academic-Industrial Partnership R01 CA166379 and Link Foundation fellowship. Thanks to Matt Gounis, Shaokuan Zheng, and Robert King at UMass Medical School for help on MRI imaging.

REFERENCES

- [1] "American cancer society: Cancer facts and figures 2018." <https://www.cancer.org/research/cancer-facts-statistics/all-cancer-facts-figures/cancer-facts-figures-2018.html>, 2018.
- [2] I. T. Gavrilovic and J. B. Posner, "Brain metastases: epidemiology and pathophysiology," *Journal of neuro-oncology*, vol. 75, no. 1, pp. 5–14, 2005.
- [3] Q. H. Li, L. Zamorano, A. Pandya, R. Perez, J. Gong, and F. Diaz, "The application accuracy of the neuromate robota quantitative comparison with frameless and frame-based surgical localization systems," *Computer Aided Surgery*, vol. 7, no. 2, pp. 90–98, 2002.
- [4] M. Eljamel, "Validation of the pathfinder neurosurgical robot using a phantom," *The International Journal of Medical Robotics and Computer Assisted Surgery*, vol. 3, no. 4, pp. 372–377, 2007.
- [5] J. Gonzalez-Martinez, S. Vadera, J. Mullin, R. Enatsu, A. V. Alexopoulos, R. Patwardhan, W. Bingaman, and I. Najm, "Robot-assisted stereotactic laser ablation in medically intractable epilepsy: operative technique," *Neurosurgery*, vol. 10, pp. 167–173, 2014.
- [6] T. Hartkens, D. L. Hill, A. D. Castellano-Smith, D. J. Hawkes, C. Maurer, A. J. Martin, W. A. Hall, H. Liu, and C. L. Truwit, "Measurement and analysis of brain deformation during neurosurgery," *IEEE Transactions on Medical Imaging*, vol. 22, no. 1, pp. 82–92, 2003.
- [7] J. L. Ostrem, N. Ziman, N. B. Galifianakis, P. A. Starr, M. San Luciano, M. Katz, C. A. Racine, A. J. Martin, L. C. Markun, and P. S. Larson, "Clinical outcomes using clearpoint interventional mri for deep brain stimulation lead placement in parkinsons disease," *Journal of neuro-surgery*, vol. 124, no. 4, pp. 908–916, 2016.

- [8] S. Song, N. Hata, I. Iordachita, G. Fichtinger, C. Tempny, and J. Tokuda, "A workspace-orientated needle-guiding robot for 3T MRI-guided transperineal prostate intervention: evaluation of in-bore workspace and MRI compatibility," *The International Journal of Medical Robotics and Computer Assisted Surgery*, vol. 9, no. 1, pp. 67–74, 2013.
- [9] E. Franco, D. Brujic, M. Rea, W. M. Gedroyc, and M. Ristic, "Needle-guiding robot for laser ablation of liver tumors under mri guidance," *IEEE/ASME Transactions on Mechatronics*, vol. 21, no. 2, pp. 931–944, 2016.
- [10] D. B. Comber, J. E. Slightam, V. R. Gervasi, J. S. Neimat, and E. J. Barth, "Design, additive manufacture, and control of a pneumatic mr-compatible needle driver," *IEEE Transactions on Robotics*, vol. 32, no. 1, pp. 138–149, 2016.
- [11] Y. Chen, I. S. Godage, Z. T. H. Tse, R. J. Webster, and E. J. Barth, "Characterization and control of a pneumatic motor for mr-conditional robotic applications," *IEEE/ASME Transactions on Mechatronics*, vol. 22, no. 6, pp. 2780–2789, 2017.
- [12] R. Seifabadi, M. Li, S. Xu, A. H. Negussie, Z. T. H. Tse, and B. J. Wood, "Mri robot for prostate focal laser ablation: a phantom study," in *Medical Imaging 2019: Image-Guided Procedures, Robotic Interventions, and Modeling*, vol. 10951, p. 109510N, International Society for Optics and Photonics, 2019.
- [13] C. Jun, S. Lim, J.-P. Wolinsky, T. Garzon-Muvdi, D. Petrisor, K. Cleary, and D. Stoianovici, "Mr safe robot assisted needle access of the brain: preclinical study," *Journal of Medical Robotics Research*, vol. 3, no. 01, p. 1850003, 2018.
- [14] Z. Dong, Z. Guo, K.-H. Lee, G. Fang, W. L. Tang, H.-C. Chang, D. T. M. Chan, and K.-W. Kwok, "High-performance continuous hydraulic motor for mr safe robotic teleoperation," *IEEE Robotics and Automation Letters*, vol. 4, no. 2, pp. 1964–1971, 2019.
- [15] Y. Kim, S. S. Cheng, M. Diakite, R. P. Gullapalli, J. M. Simard, and J. P. Desai, "Toward the development of a flexible mesoscale mri-compatible neurosurgical continuum robot," *IEEE Transactions on Robotics*, vol. 33, no. 6, pp. 1386–1397, 2017.
- [16] S. Lwu and G. R. Sutherland, "The development of robotics for interventional mri," *Neurosurgery Clinics of North America*, vol. 20, no. 2, pp. 193–206, 2009.
- [17] T. A. Mattei, A. H. Rodriguez, D. Sambhara, and E. Mendel, "Current state-of-the-art and future perspectives of robotic technology in neurosurgery," *Neurosurgical review*, vol. 37, no. 3, pp. 357–366, 2014.
- [18] R. Monfaredi, K. Cleary, and K. Sharma, "Mri robots for needle-based interventions: systems and technology," *Annals of biomedical engineering*, vol. 46, no. 10, pp. 1479–1497, 2018.
- [19] G. Li, H. Su, G. Cole, W. Shang, K. Harrington, A. Camilo, J. G. Pilitsis, G. S. Fischer, et al., "Robotic System for MRI-Guided Stereotactic Neurosurgery," *Biomedical Engineering, IEEE Transactions on*, vol. 62, no. 4, pp. 1077–1088, 2015.
- [20] J. MacDonell, N. Patel, S. Rubino, G. Ghoshal, G. Fischer, E. C. Burdette, R. Hwang, and J. G. Pilitsis, "Magnetic resonance-guided interstitial high-intensity focused ultrasound for brain tumor ablation," *Neurosurgical focus*, vol. 44, no. 2, p. E11, 2018.
- [21] G. Ghoshal, V. Salgaonkar, J. Wooton, E. Williams, P. Neubauer, L. Frith, B. Komadina, C. Diederich, and E. C. Burdette, "Ex-vivo and simulation comparison of multi-angular ablation patterns using catheter-based ultrasound transducers," in *SPIE BiOS*, pp. 85840Y–85840Y, International Society for Optics and Photonics, 2013.
- [22] S. J. Scott, P. Prakash, V. Salgaonkar, P. D. Jones, R. N. Cam, M. Han, V. Rieke, E. C. Burdette, and C. J. Diederich, "Interstitial ultrasound ablation of tumors within or adjacent to bone: Contributions of preferential heating at the bone surface," in *SPIE BiOS*, pp. 85840Z–85840Z, International Society for Optics and Photonics, 2013.
- [23] S. Eslami, W. Shang, G. Li, N. Patel, G. S. Fischer, J. Tokuda, N. Hata, C. M. Tempny, and I. Iordachita, "In-bore prostate transperineal interventions with an MRI-guided parallel manipulator: system development and preliminary evaluation," *The International Journal of Medical Robotics and Computer Assisted Surgery*, 2015.
- [24] H. Su, W. Shang, G. Cole, G. Li, K. Harrington, A. Camilo, J. Tokuda, C. M. Tempny, N. Hata, and G. S. Fischer, "Piezoelectrically-actuated robotic system for MRI-guided prostate percutaneous therapy," *Mechatronics, IEEE/ASME Transactions on*, vol. 99, no. 3, pp. 1–13, 2015.
- [25] J. Tokuda, S. Song, K. Tuncali, C. Tempny, and N. Hata, "Configurable Automatic Detection and Registration of Fiducial Frames for Device-to-Image Registration in MRI-Guided Prostate Interventions," in *Medical Image Computing and Computer-Assisted Intervention–MICCAI 2013*, pp. 355–362, Springer, 2013.
- [26] J. Tokuda, G. S. Fischer, X. Papademetris, Z. Yaniv, L. Ibanez, P. Cheng, H. Liu, J. Blevins, J. Arata, A. J. Golby, et al., "Openiglink: an open network protocol for image-guided therapy environment," *The International Journal of Medical Robotics and Computer Assisted Surgery*, vol. 5, no. 4, pp. 423–434, 2009.
- [27] "Human head." https://en.wikipedia.org/wiki/Human_head.
- [28] J. W. Young, "Head and face anthropometry of adult us civilians," tech. rep., DTIC Document, 1993.
- [29] A. Mujoomdar, J. H. Austin, R. Malhotra, C. A. Powell, G. D. Pearson, M. C. Shiau, and H. Raftopoulos, "Clinical predictors of metastatic disease to the brain from non-small cell lung carcinoma: primary tumor size, cell type, and lymph node metastases," *Radiology*, vol. 242, no. 3, pp. 882–888, 2007.
- [30] N. A. Patel, T. van Katwijk, G. Li, P. Moreira, W. Shang, S. Misra, and G. S. Fischer, "Closed-loop asymmetric-tip needle steering under continuous intraoperative MRI guidance," in *Engineering in Medicine and Biology Society (EMBC), 2015 37th Annual International Conference of the IEEE*, pp. 4869–4874, IEEE, 2015.



Gang Li Ph.D. received B.S. and M.S. degrees in Mechanical Engineering from Harbin Institute of Technology. He received the Ph.D. degree in Mechanical Engineering from Worcester Polytechnic Institute in 2016. His research interests include medical robotics, electromechanical design, and image-guided therapy. Currently he is a postdoctoral fellow at Johns Hopkins University.



Niravkumar A. Patel Ph.D. received his Bachelors degree in Computer Engineering from North Gujarat University, India and M.Tech. degree in Computer Science and Engineering in 2007 from Nirma University, India. He received the Ph.D. degree in Robotics Engineering from Worcester Polytechnic Institute in 2017. Currently he is a postdoctoral fellow at Johns Hopkins University.



Everette C. Burdette Ph.D. received the B.S. degree in physics, M.S. degree in Electrical and Electronics Engineering from Georgia Institute of Technology, and Ph.D. degree in Physiology from Emory University School of Medicine. He is the President and CEO of Acoustic MedSystems, Inc., a company developing image-guided interventions for brachytherapy, biopsy, surgery, and localized therapies using high intensity ultrasound.



Julie Pilitsis M.D., Ph.D. graduated from Albany Medical College. She completed her residency at Wayne State University, during which time she also obtained a PhD in neurophysiology. She served as director of functional neurosurgery at UMass Memorial Medical Center. She is currently Chair of the Department of Neuroscience & Experimental Therapeutics and Professor of Neurosurgery at Albany Medical College.



Hao Su Ph.D. received the B.S. degree from the Harbin Institute of Technology and M.S. degree from the State University of New York at Buffalo, and Ph.D. degree from the Worcester Polytechnic Institute. He was a research scientist at Philips Research North America and a postdoctoral fellow researcher at Harvard University. He is now an Assistant professor at City University of New York.



Gregory Fischer Ph.D. is a Professor of Mechanical Engineering with appointments in Biomedical and Robotics Engineering at Worcester Polytechnic Institute. He received B.S. degrees in Electrical and Mechanical Engineering from Rensselaer Polytechnic Institute and an M.S.E. degree in Electrical Engineering from Johns Hopkins University. He received his Ph.D. degree in Mechanical Engineering from Johns Hopkins University. He is Director of the WPI Automation and Interventional Medicine Laboratory.